Optical Fiber Technology 101 (2026) 104689

Contents lists available at ScienceDirect

Optical Fiber Technology

journal homepage: www.elsevier.com/locate/yofte

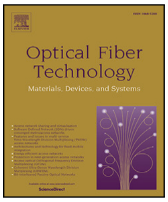

Regular Articles

A compact PDMS-enhanced fiber Fabry–Pérot sensor for micro-force measurement and material stiffness discrimination

Liqing Jing [a,b,c], Dejun Liu [b,c], Ying Wang [b,c], Changrui Liao [b,c], Cailing Fu [b,c], Yiping Wang [b,c], Chunying Guan [a,*], Weijia Bao [b,c,*]

[a] Key Laboratory of In-Fiber Integrated Optics of Ministry of Education, College of Physics and Optoelectronic Engineering, Harbin Engineering University, Harbin, 150001, China
[b] State Key Laboratory of Radio Frequency Heterogeneous Integration, Key Laboratory of Optoelectronic Devices and Systems of Ministry of Education/Guangdong Province, College of Physics and Optoelectronic Engineering, Shenzhen University, Shenzhen, 518060, China
[c] Shenzhen Key Laboratory of Ultrafast Laser Micro/Nano Manufacturing, Guangdong and Hong Kong Joint Research Centre for Optical Fibre Sensors, Shenzhen University, Shenzhen, 518060, China

ARTICLE INFO

Keywords:
Fiber Fabry–Pérot interferometer
PDMS membrane
Micro-force sensing
Stiffness discrimination
Optomechanical sensing

ABSTRACT

A compact reflection-mode fiber Fabry–Pérot (FP) sensor based on a mechanically tunable polydimethylsiloxane (PDMS) cavity is proposed for micro-force measurement and stiffness characterization. The device forms a low-finesse FP cavity between a cleaved fiber end-face and a gold-coated PDMS membrane integrated within a ceramic ferrule, providing a free spectral range on the order of several nanometers. Under axial compression, deformation of the PDMS layer modulates the cavity length, producing a clear and reversible spectral response with a force sensitivity of 0.72 nm/mN and a resolution of approximately 80 μN. The sensor exhibits a relatively fast dynamic response (0.24–0.40 s) with limited hysteresis, enabling reliable tracking of force variations. By employing PDMS layers with different mixing ratios, stiffness-dependent spectral responses are obtained for effective hardness discrimination. In addition, lateral scanning enables spatial stiffness profiling. To further improve robustness, an FBG-based temperature compensation approach is incorporated, with detailed implementation provided in the Supplementary Material. The proposed modular FP platform offers compactness, robustness, and multifunctional sensing capability.

1. Introduction

Mechanical sensing of soft materials is of great importance in applications such as soft robotics, wearable electronics, and biomedical diagnostics, where accurate force detection and mechanical characterization are essential [1,2]. Although electrical pressure and strain sensors have been widely studied, their performance can be affected by electromagnetic interference, signal drift, and long-term stability issues. Optical sensing offers an attractive alternative due to its intrinsic immunity to electromagnetic noise, high resolution, and capability for remote interrogation [3,4].

Among various optical sensing approaches, fiber-optic sensors – particularly Fiber Bragg Gratings (FBGs) and Fabry–Pérot (FP) interferometers – have attracted significant attention owing to their compact size, mechanical flexibility, and excellent compatibility with flexible and miniaturized systems [5,6]. Extrinsic fiber Fabry–Pérot interferometric (EFPI) sensors have been extensively explored for pressure, displacement, and mechanical sensing [7,8]. By employing diaphragm-based or polymer-assisted cavity structures, fiber FP sensors can achieve high sensitivity within compact configurations [9,10]. In particular, miniature fiber-tip FP cavities based on elastomeric membranes have demonstrated promising performance in micro-force and pressure sensing [11]. The modulation of cavity length under external loading provides a direct optical response to applied force, making FP-based sensors well suited for precision mechanical measurements.

However, despite these advances, most reported fiber-optic sensors primarily focus on force or pressure quantification, while quantitative discrimination of material stiffness remains insufficiently explored. Stiffness selectivity is critical for applications such as tissue mechanics evaluation, material classification, and tactile perception in soft robotic systems [12,13]. Furthermore, achieving micronewton-level force resolution within a compact and reusable fiber-integrated platform remains technically challenging [14,15]. Such a dual-function capability is particularly advantageous in applications including soft robotic manipulation, where both contact force and material stiffness are required for

---

* Corresponding authors.
E-mail addresses: cyguan@163.com (C. Guan), wjbao@szu.edu.cn (W. Bao).

https://doi.org/10.1016/j.yofte.2026.104689
Received 16 February 2026; Received in revised form 20 April 2026; Accepted 10 May 2026

accurate object recognition, as well as in biomedical diagnostics, where simultaneous force sensing and mechanical characterization can assist in tissue evaluation. In addition, this multifunctionality is beneficial for flexible electronics and soft material analysis, enabling integrated mechanical sensing within compact platforms.

To address these challenges, we propose a compact reflection-mode fiber Fabry–Pérot sensor incorporating a dual-layer polydimethylsiloxane (PDMS) structure within a ceramic ferrule. The modular architecture ensures stable cavity formation and mechanical robustness, while enabling interchangeable sensing membranes with tunable elastic properties. The proposed sensor achieves quantitative micro-force measurement with reversible spectral response under axial compression, exhibiting fast dynamic response and limited hysteresis. By employing PDMS layers with different mixing ratios, stiffness-dependent spectral responses are obtained for effective hardness discrimination. In addition, lateral scanning enables spatial stiffness profiling and detection of localized mechanical variations. Furthermore, an FBG-based temperature compensation strategy is introduced to decouple temperature and force responses, enhancing measurement accuracy under varying thermal conditions. This demonstrates that the proposed fiber FP platform provides a compact and multifunctional solution for quantitative mechanical characterization of soft materials.

2. Design and principle

The proposed device is a fiber-integrated extrinsic Fabry–Pérot (FP) interferometric sensor formed between the cleaved end face of a single-mode fiber (SMF) and a gold-coated polydimethylsiloxane (PDMS) membrane, as illustrated in Fig. 1. The PDMS layer simultaneously serves as the optical cavity medium and the mechanically deformable element, enabling direct opto-mechanical coupling within a compact fiber-based architecture.

As shown in Fig. 1(b), the incident optical field E_i is partially reflected at the fiber–PDMS interface with an effective power reflectivity R_1, while the remaining portion transmits into the PDMS cavity. During propagation, the field experiences absorption loss α_1 and accumulates a single-pass phase delay $\phi = \beta L$, where $\beta = 2\pi n/\lambda$, L is the cavity length, n is the refractive index of PDMS, and λ is the wavelength. At the PDMS–gold interface, the light is reflected with a high reflectivity $R_2 \approx 1$ and propagates back to the fiber interface, where multi-beam interference occurs.

All reflectivities and loss factors (R_1, R_2, A_1, and α_1) are defined as effective power coefficients describing reflection and attenuation in the cavity. For consistency with the schematic representation in Fig. 1(b), the reflected field amplitudes are expressed in terms of equivalent power coupling factors.

The first round-trip component reflected back into the fiber is given by

$$E_r^{(1)} = (1 - R_1)(1 - A_1)(1 - \alpha_1)E_i e^{-j2\phi}. \tag{1}$$

For each additional round-trip within the cavity, the field acquires an additional attenuation factor and phase delay. The round-trip attenuation factor is

$$r = R_1(1 - A_1)^2(1 - \alpha_1)^2 e^{-j2\phi}. \tag{2}$$

Thus, the nth order reflected component can be written as

$$E_r^{(n)} = E_r^{(1)} r^{n-1}. \tag{3}$$

By summing all round-trip contributions, the total reflected field becomes

$$E_r = \sum_{n=1}^{\infty} E_r^{(n)} = \frac{(1 - R_1)(1 - A_1)(1 - \alpha_1)E_i e^{-j2\phi}}{1 - R_1(1 - A_1)^2(1 - \alpha_1)^2 e^{-j2\phi}}. \tag{4}$$

The measurable reflected intensity is proportional to the square modulus of the reflected field:

$$|E_r|^2 = \frac{(1 - R_1)^2(1 - A_1)^2(1 - \alpha_1)^2|E_i|^2}{1 + R_1^2(1 - A_1)^4(1 - \alpha_1)^4 - 2R_1(1 - A_1)^2(1 - \alpha_1)^2\cos(4\beta L)}. \tag{5}$$

Under the low-loss and low-finesse approximation [16], Eq. (5) reduces to the standard Airy-type interference response of a Fabry–Pérot cavity [17].

The interference follows the standard Fabry–Pérot condition. The corresponding free spectral range (FSR) is approximately

$$\Delta\lambda \approx \frac{\lambda^2}{2nL}. \tag{6}$$

The sensing mechanism originates from elastic deformation of the PDMS membrane. Under external mechanical loading, the cavity length varies by ΔL, resulting in a phase perturbation

$$\Delta\phi = \frac{4\pi n}{\lambda}\Delta L. \tag{7}$$

Since the deformation magnitude depends on the effective Young's modulus E of the PDMS layer, different stiffness values produce distinct cavity-length variations under identical loading conditions [18,19]. This establishes a direct mapping between mechanical stiffness and optical phase modulation, forming the theoretical basis for stiffness-sensitive tactile detection.

In addition to mechanical deformation, the optical path length of the PDMS-based Fabry–Pérot cavity may also be influenced by temperature variations. Owing to the relatively large thermal expansion coefficient and thermo-optic coefficient of PDMS, both the cavity length L and the refractive index n may vary with temperature, which can introduce an additional phase shift and consequently lead to spectral drift. Therefore, the measured wavelength response should be understood as predominantly deformation-induced under stable laboratory conditions, while temperature fluctuations may act as a secondary perturbation. In practical applications, such temperature cross-sensitivity can be mitigated by calibration or compensation strategies, such as reference structures or differential interrogation. To further improve measurement robustness under varying thermal conditions, an FBG-based temperature compensation approach was implemented. The detailed configuration, theoretical derivation, and experimental validation are provided in the Supplementary Material.

3. Fabrication and characterization

The fabrication process of the micro-force sensor is schematically illustrated in Fig. 2(a). A single-mode optical fiber was inserted into a ceramic ferrule, with the fiber tip protruding approximately 40 μm beyond the ferrule end to form the initial optical interface. As shown in Fig. 3(a), the corresponding reflection spectrum exhibits only weak Fresnel reflection at the fiber–air boundary, without observable interference features, indicating the absence of a defined cavity structure.

To obtain a highly compliant and pressure-sensitive microcavity, the base-to-curing-agent ratio of the PDMS was set to 1:20 [20]. The Young's modulus of PDMS varies significantly with the precursor-to-curing-agent ratio, typically ranging from tens of kPa to several MPa, as reported in the literature. The elevated base content reduces crosslink density, resulting in a lower elastic modulus and enhanced deformability of the sensing membrane. The effective Young's modulus of PDMS is strongly dependent on the base-to-curing-agent ratio. A higher curing-agent content leads to increased crosslinking density and thus a higher elastic modulus, resulting in reduced deformation under the same applied force. A controlled droplet of the uncured PDMS was dispensed onto the ferrule tip and thermally cured at 120 °C for 90 s, forming a hemispherical membrane with an average thickness of approximately 86 μm (Fig. 2(b)). The introduction of this PDMS layer establishes a secondary reflection surface at the PDMS–air interface, resulting in the emergence of weak interference fringes in the reflection spectrum (Fig. 3(b)). This high-ratio PDMS layer functions as the primary deformable sensing element.

To enhance cavity reflectivity and improve fringe contrast, a gold film with a thickness of approximately 120 nm was laminated onto the PDMS surface (Fig. 2(c)). The gold layer serves as a high-reflectance

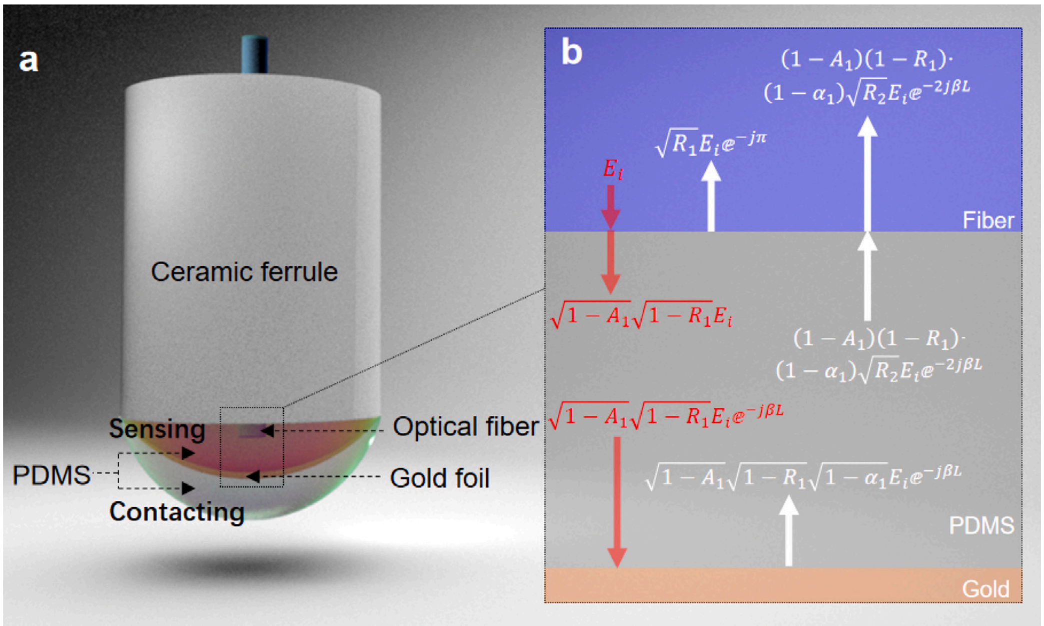

Fig. 1. Schematic and interference mechanism of the fiber–PDMS Fabry–Pérot sensor.

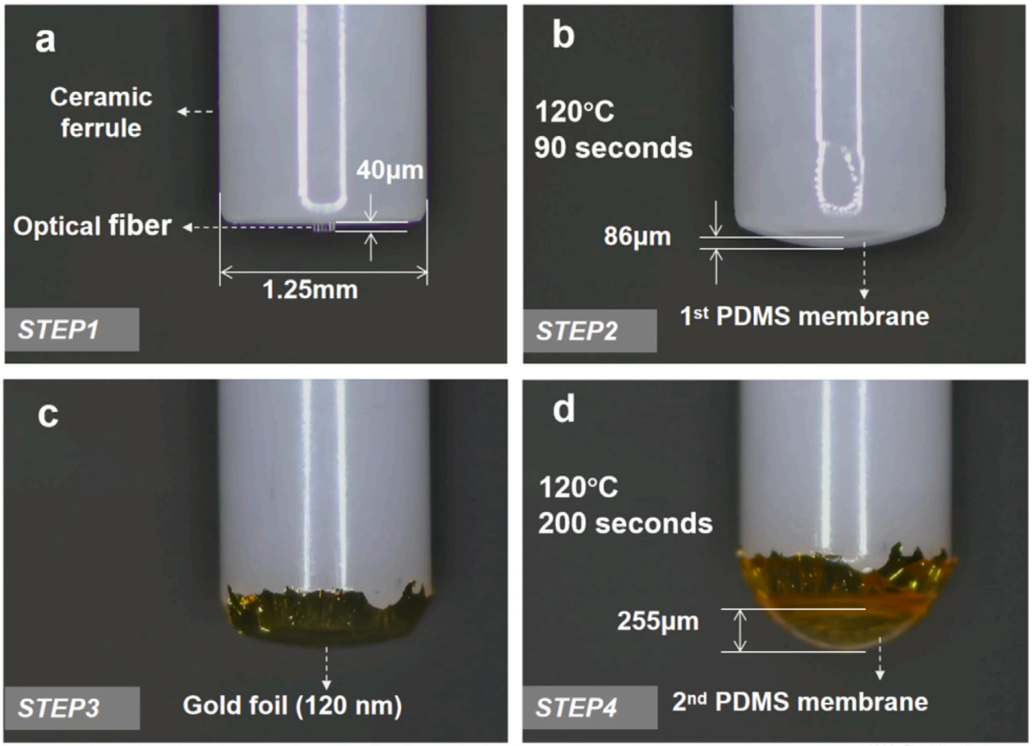

Fig. 2. Fabrication of the modular fiber–PDMS–gold Fabry–Pérot sensor. (a) The SMF protrudes by approximately 40 μm from the ceramic ferrule. (b) A ~ 86 μm PDMS layer is deposited and cured at 120 °C for 90 s. (c) A ~ 120 nm gold foil is applied to form the reflective interface. (d) A second PDMS encapsulation layer (total PDMS thickness ~ 255 μm) is added and cured for 200 s.

mirror at the cavity boundary. As shown in Fig. 3(c), the introduction of the gold film significantly enhances the fringe visibility and increases the overall reflected intensity, while the free spectral range (FSR) remains nearly unchanged.

According to the standard Fabry–Pérot relation $\Delta\lambda \approx \lambda^2/(2nL)$, the measured FSR corresponds to an effective cavity length on the order of tens of micrometers (assuming $n \approx 1.4$), which is consistent with the experimentally estimated PDMS thickness. The preservation of the FSR indicates that the effective cavity length is not significantly altered by the gold-film integration, whereas the improved fringe contrast suggests an increase in the effective cavity reflectivity and finesse.

Subsequently, to form a mechanically robust sensing contact layer with higher stiffness, the PDMS base-to-curing-agent ratio was adjusted to 1:5 [21]. The increased curing-agent content promotes crosslinking, leading to reduced compliance and improved structural rigidity. This lower-elasticity PDMS was dispensed over the gold-coated surface and

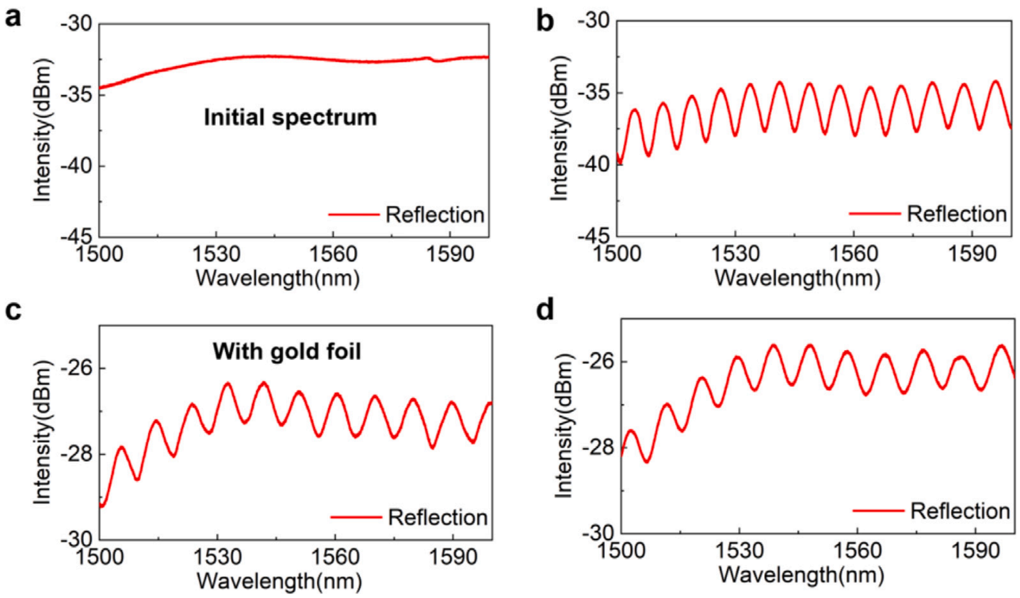

Fig. 3. Reflection spectra at key fabrication steps. (a) bare SMF; (b) after PDMS membrane casting; (c) with gold reflector; (d) final PDMS encapsulation.

cured at 120 °C for 200 s, fully encapsulating the reflective interface (Fig. 2(d)). After encapsulation, the total PDMS thickness increased to approximately 255 μm. The final reflection spectrum (Fig. 3(d)) exhibits strong and stable interference fringes with high visibility, confirming the formation of a fully enclosed low-finesse Fabry–Perot cavity.

It should be noted that the cavity geometry is primarily determined by the dispensed PDMS volume, fiber protrusion length, and curing conditions. In this work, the PDMS droplet volume was controlled using a fixed-volume micropipette, while the fiber alignment and protrusion length were maintained using a mechanical positioning fixture. These measures help improve fabrication consistency and reduce operator-dependent variations. Although slight device-to-device variations may arise from the droplet-based fabrication process, the measured spectra consistently exhibit a well-defined Fabry–Pérot response with a similar free spectral range, indicating that the effective cavity length remains within a reasonably controlled range.

4. Sensing performance and discussion

4.1. Micro-force calibration

To investigate the mechanical-to-optical transduction behavior of the proposed fiber–PDMS–gold Fabry–Pérot sensor, controlled compressive loading experiments were conducted. The fabricated device (Fig. 4(a,b)), approximately 7 mm in length and 1 mm in diameter, was mounted on a precision translation stage (Newport GTS30V). The reflection spectrum was monitored using a fiber-optic interrogator (MOI SI255), while a microbalance positioned beneath the sensor enabled quantitative force measurement (Fig. 4(c)). As the translation stage advanced in 1 μm increments, the sensor gradually contacted a flat plate and experienced progressive compression. This deformation induces a clear blue shift of the interference spectrum (Fig. 4(d)). The wavelength shift was determined by tracking the positions of interference extrema in the reflection spectrum, where the peak wavelengths were extracted from the spectral response under different loading conditions. The spectral shift arises from cavity-length reduction, which induces a phase variation $\Delta\phi = \frac{4\pi n}{\lambda}\Delta L$ according to the interference model established in Section 2.

The relationship between pressing depth and applied force is shown in Fig. 5(a), demonstrating excellent linearity ($R^2 = 0.999$). Representative reflection spectra under three discrete compressive forces (400, 850, and 1100 μN) are presented in Fig. 5(b). The interference fringes shift uniformly toward shorter wavelengths with increasing force, while maintaining consistent fringe spacing and visibility. The preserved free spectral range confirms that the cavity structure remains intact during compression, and the spectral modulation primarily results from elastic cavity-length variation rather than structural distortion.

The wavelength shift as a function of applied force is plotted in Fig. 5(c). A quadratic dependence is observed, reflecting the nonlinear elastic deformation behavior of PDMS under compressive loading. Since the cavity-length change is proportional to mechanical strain, and the optical phase scales linearly with ΔL, the nonlinear mechanical response of the polymer membrane naturally translates into a nonlinear spectral shift. This behavior is consistent with previously reported elastomer-based FP micro-force sensors. The observed nonlinear relationship between wavelength shift and applied force arises from both the intrinsic nonlinear elastic behavior of PDMS and the geometric deformation of the curved sensing membrane. As the applied force increases, the deformation of the PDMS layer becomes progressively nonlinear, leading to a non-proportional variation in cavity length and thus wavelength shift.

4.2. Repeatability and dynamic response

The repeatability of the device was evaluated through loading–unloading cycles, as shown in Fig. 5(d). During force increase and subsequent release, the wavelength response exhibits good reversibility with a small separation between the loading and unloading traces, indicating slight hysteresis behavior. The slight hysteresis originates from the viscoelastic behavior of PDMS. Within the investigated force range, the hysteresis remains limited and does not affect the overall monotonic relationship between the applied force and wavelength shift. To further quantify the dynamic response of the sensor, the response time was evaluated based on the step transitions in the loading process. As shown in Fig. 6(a), a representative force step from 260–470 μN is selected for analysis. The response time is defined as the time required for the wavelength shift to increase from 10% to 90% of its steady-state value, yielding a value of approximately 0.34 s. In addition, the response times for multiple force steps, including 0–140 μN, 140–260 μN, 260–470 μN, 470–620 μN, 620–1000 μN, and 1000–1200 μN, were extracted and summarized in Fig. 6(b). The results show that the response time varies within the range of 0.24–0.40 s, with an average value of approximately

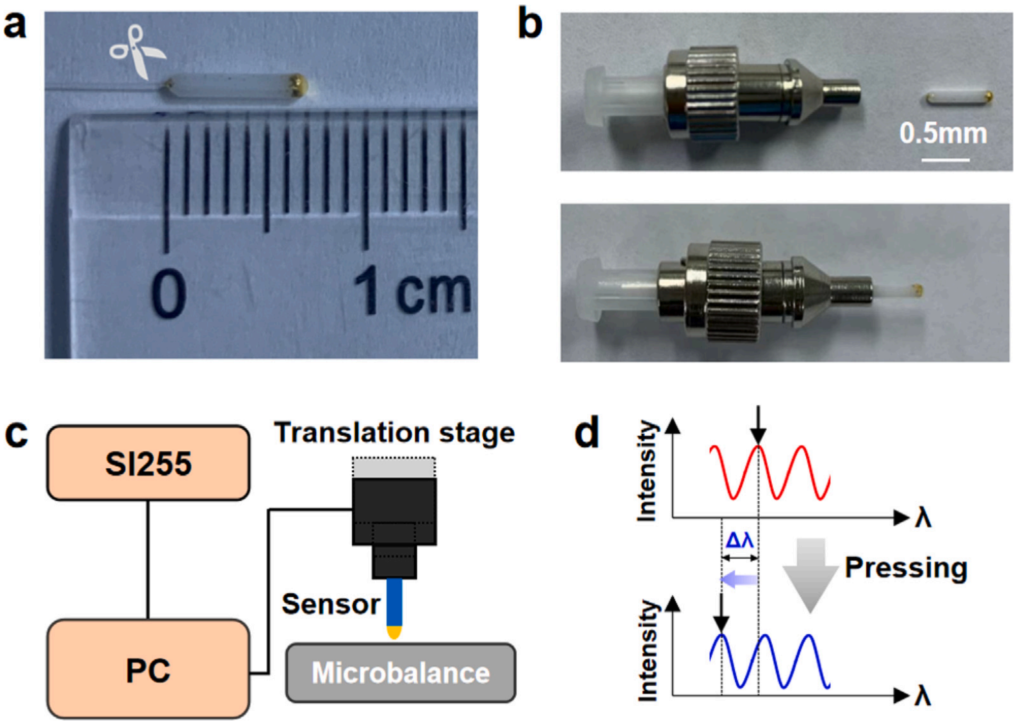

Fig. 4. Experimental setup for mechanical loading and spectral measurement. (a) Ceramic ferrule-based fiber module (~ 0.7 cm). (b) Mounting into standard metallic flange. (c) Axial loading using translation stage and flat-tip probe. (d) Reflection spectra under increasing compressive forces.

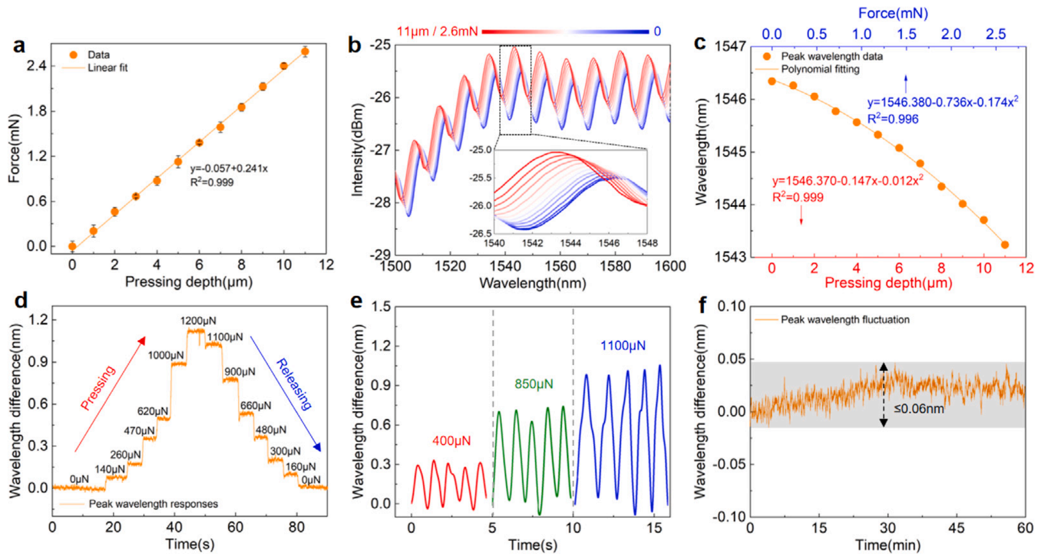

Fig. 5. Mechanical calibration and spectral response of the fiber–PDMS FP sensor. (a) Force–displacement curve of the PDMS dome under axial loading. (b) Reflection spectra under 400, 850, and 1100 μN compressive force. (c) Wavelength shift as a function of insertion depth with polynomial fitting. (d) Dynamic load–unload response of the sensor. (e) Comparison of wavelength shifts under three discrete force levels. (f) Spectral stability over 60 min under constant load.

0.30 s. These results indicate that the sensor exhibits a relatively fast and consistent dynamic response across different force levels.

To further evaluate the dynamic tracking capability, vibration-induced tapping tests were carried out. Consistent spectral modulation was observed across multiple force levels (400, 850, and 1100 μN), confirming robust mechanical coupling at the fiber–PDMS interface and the ability of the sensor to follow repeated force variations.

Due to the viscoelastic properties of PDMS, the response exhibits rate-dependent behavior, as reflected by the variation in response time (0.24–0.40 s). Therefore, the dynamic response of the sensor is intrinsically rate-dependent, which should be considered in practical applications, especially under high-speed or time-resolved conditions.

Long-term stability was further examined under constant loading for 60 min (Fig. 5(f)). The spectral fluctuation remained below 0.06 nm. The fluctuation mainly reflects the short-term stability of the enclosed cavity structure under stable laboratory conditions. Based on the calibration results in Fig. 5(c), the force sensitivity S_F is determined to be 0.72 nm/mN under stable temperature conditions. Accordingly, the force resolution, estimated as $\Delta\lambda_{\text{noise}}/S_F$, is approximately 80 μN. The

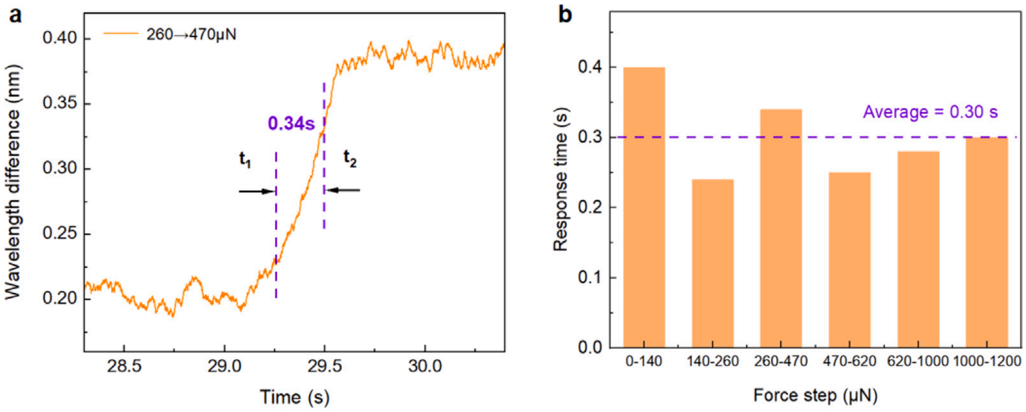

Fig. 6. Dynamic response analysis of the fiber–PDMS FP sensor. (a) Dynamic response of the sensor for a representative force step (260–470 μN), showing a response time of ~0.34 s (10%–90%). (b) Response time for different force ranges, indicating consistent performance within 0.24–0.40 s (average ~0.30 s).

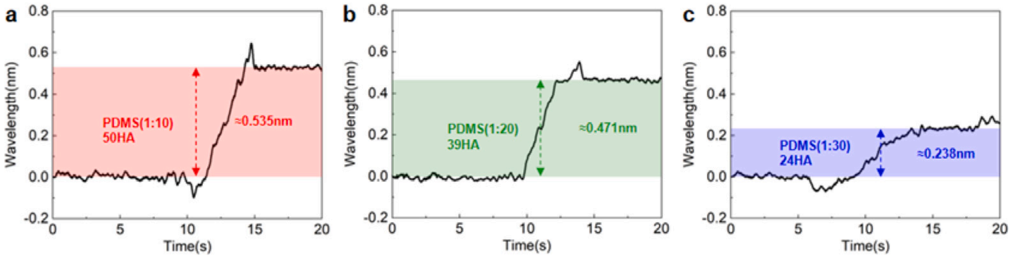

Fig. 7. Spectral response of the Fabry–Pérot sensor to PDMS layers with different stiffness levels (a) PDMS (1:10), Shore A 50, wavelength shift ~ 0.530 nm. (b) PDMS (1:20), Shore A 39, shift ~ 0.471 nm. (c) PDMS (1:30), Shore A 24, shift ~ 0.238 nm. These results confirm a consistent correlation between PDMS stiffness and the resulting optical response.

high signal stability can be attributed to the enclosed cavity configuration and enhanced reflectivity at the PDMS–gold interface, which suppress environmental perturbations and improve fringe contrast. In addition, the signal-to-noise ratio of the measurement is improved by the high fringe visibility, while the use of a stable broadband light source minimizes spectral fluctuation.

4.3. Hardness discrimination

Beyond micro-force sensing, the device was evaluated for material stiffness discrimination. PDMS samples with precursor-to-curing-agent ratios of 1:10, 1:20, and 1:30 were prepared under identical curing conditions. The corresponding Shore A hardness values were measured to be 50, 39, and 24 HA, respectively.

As shown in Fig. 7, the spectral shift amplitude increases with increasing material stiffness. Under identical indentation depth, stiffer materials generate larger reaction forces, leading to greater cavity compression and enhanced phase modulation. In contrast, softer samples undergo larger local deformation with reduced reaction force, resulting in smaller spectral shifts. The monotonic correlation between hardness level and wavelength shift confirms the sensor's capability for stiffness-dependent discrimination. Although PDMS samples with different mixing ratios are used here as representative test materials, the proposed sensing approach is not limited to PDMS. Since the sensing mechanism relies on deformation-induced cavity-length modulation and the corresponding reaction force under contact loading, it can be extended to other soft or heterogeneous materials with different elastic properties.

4.4. Spatial stiffness profiling

To further demonstrate spatial mechanical mapping capability, a composite sample consisting of a PMMA mold embedded with glass rods inside a PDMS matrix was fabricated (Fig. 8(a)). The sensor was mounted on a two-axis translation stage and scanned laterally with a step size of 3 μm (Fig. 8(b)).

The resulting spectral response map (Fig. 8(c)) clearly reveals regions corresponding to pure PMMA (higher stiffness), pure PDMS (lower stiffness), and glass-embedded zones (locally elevated stiffness). When the sensor contacted pure PMMA regions, pronounced spectral shifts were observed due to higher indentation resistance. In contrast, pure PDMS regions produced smaller shifts. The glass inclusions increased the effective local stiffness within the PDMS matrix, resulting in intermediate spectral modulation.

The ability to resolve localized stiffness variations highlights the potential of the proposed fiber-integrated FP sensor for micro-scale mechanical profiling in soft materials, flexible electronics, and tactile sensing applications.

5. Conclusion

A compact and reconfigurable fiber-integrated Fabry–Pérot (FP) sensor based on a PDMS cavity is demonstrated. The ferrule-assisted architecture ensures mechanical robustness and enables modular integration within standard fiber-optic systems.

Quantitative micro-force measurement is achieved through calibration of the force–wavelength response, exhibiting high resolution, good reversibility, and limited hysteresis. The sensor also shows a fast and consistent dynamic response, with a response time of 0.24–0.40 s (average ~0.30 s), enabling reliable tracking of force variations.

By employing PDMS layers with different mixing ratios, stiffness-dependent spectral responses are obtained, allowing effective hardness discrimination. In addition, lateral scanning enables spatial stiffness profiling, demonstrating the capability to resolve localized mechanical variations.

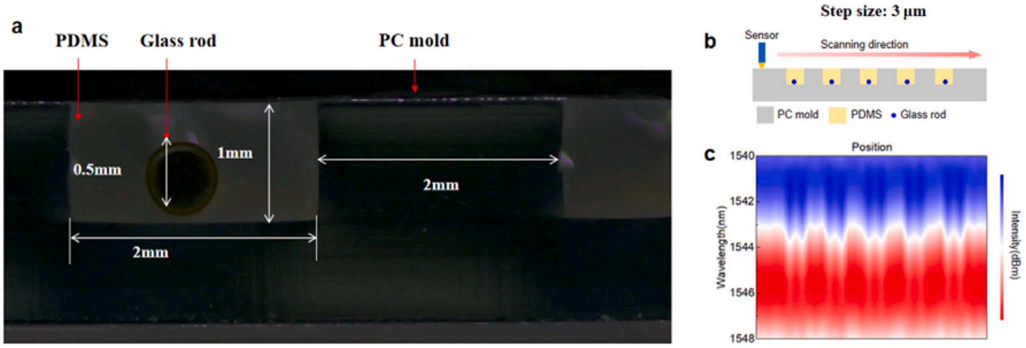

Fig. 8. Spatial stiffness profiling using Fabry–Pérot spectral scanning (a) Microscope image of the composite PDMS sample. (b) Schematic of lateral scanning configuration (step size 3 μm). (c) 2D spectral and intensity map revealing localized stiffness variations across embedded structures.

To improve measurement robustness under practical conditions, an FBG-based temperature compensation strategy is introduced, with detailed implementation provided in the Supplementary Material, thereby enhancing measurement accuracy in thermally varying environments.

Overall, the proposed sensor integrates micro-force measurement, dynamic response, stiffness discrimination, spatial mapping, and temperature compensation within a compact fiber platform, showing strong potential for applications in soft robotics, flexible electronics, and biomedical sensing.

CRediT authorship contribution statement

Liqing Jing: Writing – review & editing, Writing – original draft, Resources, Investigation, Formal analysis, Data curation, Conceptualization. **Dejun Liu:** Investigation. **Ying Wang:** Software, Resources. **Changrui Liao:** Investigation, Funding acquisition. **Cailing Fu:** Formal analysis, Conceptualization. **Yiping Wang:** Investigation, Funding acquisition, Formal analysis. **Chunying Guan:** Supervision, Software, Investigation, Formal analysis, Data curation, Conceptualization. **Weijia Bao:** Writing – original draft, Software, Resources, Methodology, Investigation, Funding acquisition, Formal analysis, Data curation, Conceptualization.

Declaration of competing interest

The authors declare that they have no known competing financial interests or personal relationships that could have appeared to influence the work reported in this paper.

Acknowledgments

This work was supported by the National Key Research and Development Program of China (Grant No. 2024YFB3213700) and the National Natural Science Foundation of China (Grant Nos. T2421003 and U22A2088).

Appendix A. Supplementary data

Supplementary material related to this article can be found online at https://doi.org/10.1016/j.yofte.2026.104689.

Data availability

Data will be made available on request.

References

[1] D. Rus, M.T. Tolley, Design, fabrication and control of soft robots, Nature 521 (7553) (2015) 467–475.
[2] D.-H. Kim, R. Ghaffari, N. Lu, J.A. Rogers, Flexible and stretchable electronics for biointegrated devices, Annu. Rev. Biomed. Eng. 14 (1) (2012) 113–128.
[3] Y. Chen, et al., Recent progress in MEMS fiber-optic Fabry–Perot pressure sensors, Sensors 24 (2024) 1079.
[4] X. Li, et al., A review of wearable optical fiber sensors for rehabilitation monitoring, Sensors 24 (2024) 3602.
[5] S. Xu, et al., Fiber Bragg grating pressure sensors: a review, Opt. Eng., Bellingham 62 (2023) 010902.
[6] Y.-J. Rao, In-fibre Bragg grating sensors, Meas. Sci. Technol. 8 (4) (1997) 355–375.
[7] C. Zhu, H. Zheng, L. Ma, Z. Yao, B. Liu, J. Huang, Y. Rao, Advances in fiber-optic extrinsic Fabry–Perot interferometric physical and mechanical sensors: A review, IEEE Sensors J. 23 (7) (2023) 6406–6426.
[8] Q. Yu, X. Zhou, Pressure sensor based on the fiber-optic extrinsic Fabry-Perot interferometer, Photonic Sensors 1 (1) (2011) 72–83.
[9] X. Liu, I.I. Iordachita, X. He, R.H. Taylor, J.U. Kang, Miniature fiber-optic force sensor based on low-coherence Fabry-Pérot interferometry for vitreoretinal microsurgery, Biomed. Opt. Express 3 (5) (2012) 1062–1076.
[10] Q.Y. Wang, Z.H. Ma, Polymer diaphragm based fiber optic Fabry-Perot acoustic sensor, Appl. Mech. Mater. 401 (2013) 1087–1090.
[11] F. Liu, S. Ren, G. Wang, X. Cai, T. Cai, PDMS diaphragm based miniature fiber-optic Fabry–Perot dynamic pressure sensor for turbomachinery application, Appl. Opt. 63 (7) (2024) 1744–1752.
[12] J. Kang, S. Lee, Y.-L. Park, Soft bending actuator with fiber-jamming variable stiffness and fiber-optic proprioception, IEEE Robot. Autom. Lett. 8 (11) (2023) 7344–7351.
[13] Q. Liu, X. Li, D. Wang, H. Gao, D. Yu, Theoretical model and design of highly sensitive reflective fiber optic Fabry-Pérot cavity accelerometer independent of fiber stiffness, IEEE Sensors J. 24 (5) (2024) 5959–5965.
[14] Y. Wei, Q. Xu, An overview of micro-force sensing techniques, Sensors Actuators A: Phys. 234 (2015) 359–374.
[15] A. Godet, J. Chretien, K.P. Huy, J.-C. Beugnot, Micronewton nanofiber force sensor using Brillouin scattering, Opt. Express 30 (2) (2022) 815–824.
[16] B. Nowakowski, D. Smith, S. Smith, Highly compact fiber Fabry-Perot interferometer: A new instrument design, Rev. Sci. Instrum. 87 (11) (2016).
[17] M. Born, E. Wolf, Principles of Optics: Electromagnetic Theory of Propagation, Interference and Diffraction of Light, Elsevier, 2013.
[18] M. Litwinowicz, S. Rogers, A. Caruana, C. Kinane, J. Tellam, R. Thompson, Tuning the bulk and surface properties of PDMS networks through cross-linker and surfactant concentration, Macromolecules 54 (20) (2021) 9636–9648.
[19] A.M. Smith, D.G. Inocencio, B.M. Pardi, A. Gopinath, R.C. Andresen Eguiluz, Facile determination of the Poisson's ratio and Young's modulus of polyacrylamide gels and polydimethylsiloxane, ACS Appl. Polym. Mater. 6 (4) (2024) 2405–2416.
[20] K. Khanafer, A. Duprey, M. Schlicht, R. Berguer, Effects of strain rate, mixing ratio, and stress–strain definition on the mechanical behavior of the polydimethylsiloxane (PDMS) material as related to its biological applications, Biomed. Microdevices 11 (2) (2009) 503–508.
[21] Y. Huang, K. Choi, C.H. Hidrovo, et al., The improved resistance of PDMS to pressure-induced deformation and chemical solvent swelling for microfluidic devices, Microelectron. Eng. 124 (2014) 66–75.